ACS APPLIED MATERIALS & INTERFACES

Research Article

www.acsami.org

Highly Ordered, Accessible and Nanocrystalline Mesoporous TiO_2 Thin Films on Transparent Conductive Substrates

Ianina L. Violi, M. Dolores Perez,† M. Cecilia Fuertes, and Galo J. A. A. Soler-Illia*

Gerencia Química, Centro Atómico Constituyentes, Comisión Nacional de Energía Atómica, Av. Gral. Paz 1499, B1650KNA, San Martín, Buenos Aires, Argentina

Supporting Information

ABSTRACT: Highly porous ($V_{mesopore}$ = 25−50%) and ordered mesoporous titania thin films (MTTF) were prepared on ITO (indium tin oxide)-covered glass by a fast two-step method. The effects of substrate surface modification and thermal treatment on pore order, accessibility and crystallinity of the MTTF were systematically studied for MTTF deposited onto bare and titania-modified ITO. MTTF exposed briefly to 550 °C resulted in highly ordered films with grid-like structures, enlarged pore size, and increased accessible pore volume when prepared onto the modified ITO substrate. Mesostructure collapse and no significant change in pore volume were observed for MTTF deposited on bare ITO substrates. Highly crystalline anatase was obtained for MTTF prepared on the modified-ITO treated at high temperatures, establishing the relationship between grid-like structures and titania crystallization. Photocatalytic activity was maximized for samples with increased crystallization and high accessible pore volume. In this manner, a simple way of designing materials with optimized characteristics for optoelectronic applications was achieved through the modification of the ITO surface and a controlled thermal treatment.

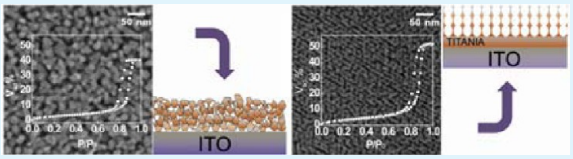

KEYWORDS: *nanocrystalline, titania, mesoporous, thin films, ITO, photocatalytic activity*

INTRODUCTION

Mesoporous titania thin films (MTTF) with crystalline framework, high pore volume and surface area, and tunable pore size have received significant attention due to their relevant applications in photocatalysis,[1,2] energy storage and conversion,[3−9] electrochromism and sensors.[10,11] A successful use of MTTF in these advanced technologies depends greatly on film features such as pore order, accessibility, and connectivity, as well as the crystallinity of the inorganic wall.[12,13] These aspects are tightly related to each other, and most attempts to modify one characteristic will influence the others.[14−16] Fine tuning of the MTTF features is a great challenge and all efforts dedicated to the exploration of the properties interdependence are highly relevant for practical applications.[17]

Nanocrystalline anatase titania is desired for photocatalytic or optoelectronic applications of MTTF, since it offers the proper energetics (E_g) for pollutant degradation in photocatalysis. Charge transport and lifetime are also enhanced by an extensive crystallization that at the same time diminishes the charge trap concentration at the grain boundaries. Photocatalysis is also favored by the mesostructure order and pore accessibility and size due to an improved molecular diffusion into the active surface centers. An increase of the photocatalytic activity has been observed for ordered mesoporous films with respect to films with textural porosity.[13−15,17,18] In addition, cubic mesostructures have shown an enhanced molecular accessibility compared to those presenting 2D-hexagonal channels.[12] The combined presence of wall crystallinity, high mesopore volume and open pore interconnection is fundamental to optimize film photocatalytic performance. Analogous attributes are required for photovoltaic applications such as Grätzel-type or all-solid state solar cells, for which MTTF have an enormous potential. Superior electron collection and reduced charge trapping are crucial to reduce the resistivity across the titania layers. In addition, an ordered mesostructure provides a large, accessible surface area that increases the organic−inorganic interactions and therefore, the charge transfer active sites.[3,12,14−16,18−24]

In order to obtain MTTF with high crystallinity, large pore size, connectivity and accessibility while maintaining an organized mesostructure, film postsynthesis thermal treatment must be carefully controlled.[12,14,15,17,18] Crystallite nucleation and growth begins around 250−300 °C on silicon substrates, followed by an extensive growth at T > 350 °C. A high porosity can be attained under the condition that crystallite growth is confined to the pore wall thickness.[25−27] For temperatures above 600 °C, extensive wall densification and massive crystallite growth leads to a progressive destruction of the pore mesostructure.[14,28,29] In addition, it has been well established that crystallinity and mesostructure pore order are dependent on the choice of the substrate, which influences the deposition and thermal evolution processes.[15,21,30]

To the best of our knowledge, the reproducible development of ordered, highly porous and nanocrystalline MTTF on transparent conducting electrodes like ITO (indium tin oxide)-covered glass is still a bottleneck for optoelectronic applications. A transparent substrate is needed for photocatalysis or

Received: June 2, 2012
Accepted: July 19, 2012
Published: July 23, 2012

 © 2012 American Chemical Society dx.doi.org/10.1021/am300990p | ACS Appl. Mater. Interfaces 2012, 4, 4320−4330

photovoltaic applications, since illumination can be carried out either from the top or the bottom of the film. While many reports describe the preparation of crystalline and ordered mesoporous titania,[31−38] no systematic work about reproducible preparation of accessible MTTF onto transparent electrode materials has been yet conducted. Crystalline MTTF are difficult to obtain on ITO because of impurities diffusion into the film during the annealing stages, and the mesostructure is practically collapsed for long thermal treatments above 500 °C.[15] The inclusion of a nonmesoporous titania buffer layer helps to improve crystallization as well as substrate wetting. Even if this concept has been presented in recent literature,[15,22,30] a need exists to understand the thermal evolution of porosity and mesostructure on bare or modified transparent substrates for several applications. This comprehension is essential to develop fast, reliable, and sound thermal treatment protocols for optimized MTTF-conductive substrate systems.

This work presents and discusses the essential aspects for the reproducible preparation of highly organized, large pore and nanocrystalline MTTF with highly accessible grid-like mesostructure onto ITO-covered glass. Films were exposed to different thermal treatments to understand the temperature effect on relevant parameters such as: mesostructure order; pore volume, size, accessibility and connectivity; and wall crystallinity. Keeping in mind future potential applications in optoelectronic devices, a thin layer of nonmesoporous titania layer was introduced as an interfacial layer (buffer) between the ITO and the mesoporous film. The dense layer modifies the ITO surface preventing ion migration from the ITO into the mesoporous framework and favoring anatase crystallite growth. In addition, the dense layer prevents charge recombination at the ITO-organic interface in the case of photovoltaic applications, thus reducing photocurrent losses. The films were thoroughly characterized using electron microscopy, X-ray diffraction and environmental ellipsometric porosimetry (EEP).[29,39] The photocatalytic activity observed is highly dependent on the substrate pretreatment and the thermal treatment carried out, demonstrating the dramatic impact of the mesostructure and crystallinity in a real world application.

EXPERIMENTAL SECTION

MTTF Synthesis. Dense and mesoporous TiO_2 thin films were deposited on ITO-covered glass substrates of 2.5 × 5 cm^2 (Thin film Devices, USA, sheet resistance 20 ± 5 ohm/sq) using dip-coating, from ethanol−water solutions containing a titania precursor; in the case of mesoporous films, a supramolecular pore template (Pluronics F127) was added.

Preparation of Initial Solutions. Titania solutions were prepared using $TiCl_4$ (Sigma Aldrich) as the inorganic source. Initially, an ethanolic solution was prepared using a Ti:EtOH (1:40 molar ratio, EtOH purchased from Merck). For the synthesis of nonporous layers, 1.80 g of Milli-Q H_2O was added to 20 g of the initial solution, giving a final molar ratio of 1 Ti/40 EtOH/10 H_2O. The mesoporous precursor solution was prepared using the previously described solution with the addition of the triblock copolymer Pluronic F127 (Sigma MW = 13 600) as a pore directing agent. The final molar ration in this case was 1 Ti/40 EtOH/10 H_2O/5 × 10^{-3} F127.

Film Synthesis. ITO substrates were washed using acetone, deionized water, and ethanol and further dried using a clean air current.

Nonporous titania (named D for "dense") were prepared by dip coating at a constant withdrawal rate of 1 mm s^{-1} under controlled relative humidity (RH) of 20%. After deposition, the films were stabilized for 30 min at 60 °C and finally calcined at 350 °C with a thermal ramp of 1 °C min^{-1} for two hours. Further thermal treatment on specific films involved exposure to 500 °C for 60 min. Even though a slight microporosity may exist for these layers,[40] nonmesoporous films will be called "dense layer" for future reference.

The F127-templated titania mesoporous layers (labeled M for "mesoporous") were prepared by dip coating at a constant withdrawal rate of 2 mm s^{-1} under controlled 35% RH. The solution was maintained at ∼35 °C to improve the substrate wettability.[41] After coating, films were placed in a 50% RH chamber for 24 h, and followed by 24 h at 60 °C, 24 h at 130 °C and a final calcination at 350 °C for two hours (thermal ramp of 1 °C min^{-1}).[42] Some films were further treated at 550 °C for 30 min with a "flash" type treatment.[28] MTTF onto dense TiO_2/ITO substrates were exposed to slightly higher temperatures than MTTF onto bare ITO to compensate for the shorter time exposure. All the thermal treatments were done in a furnace (INDEF, Córdoba, Argentina) under a still air atmosphere.

Different combinations of mesoporous and dense layers were prepared as described as follows: Monolayers ITO/D treated at 350 °C (D3), ITO/D treated at 500 °C (D5), ITO/M treated at 350 °C (M3), ITO/M treated at 550 °C (M5); Bilayers ITO/D treated at 350 °C/M treated at 350 °C (D3M3), ITO/D treated at 350 °C/M treated at 550 °C (D3M5), ITO/D treated at 500 °C/M treated at 350 °C (D5M3), ITO/D treated at 500 °C/M treated at 550 °C (D5M5).

Thin Film Characterization. *X-ray Reflectometry (XRR).* X-ray reflectometry measurements were performed at the D10A-XRD2 beamline of Laboratório Nacional de Luz Síncrotron (LNLS), Campinas, SP, Brazil, using a six circles Huber diffractometer (λ = 1.5498 Å). Thickness was obtained directly from the Kiessig fringes.[43,44] The scans were performed in the angular range between 0.15 and 3°θ, in specular mode.

Spectroscopic Ellipsometry (SE). The optical properties of TiO_2 thin films were measured by spectroscopic ellipsometry (SE SOPRA GES5A). Film thickness and refractive index values (i.e., $\bar{n}(\lambda) = n(\lambda) + ik(\lambda)$, where $n(\lambda)$ and $k(\lambda)$ are the real and imaginary components of the refractive index, respectively) were obtained from the ellipsometric parameters $\Psi(\lambda)$ and $\Delta(\lambda)$.[45] Thickness measurements previously obtained by XRR and field-emission scanning electronic microscopy (FE-SEM) were used as seeds to model the ellipsometric data.

The modeling procedure consists in fitting a multilayered system in a layer by layer fashion (see Supporting Information, Figure S1). The ITO layer was fitted using the SOPRA database parameters (modified Cauchy dispersion law, $n(\lambda) = A + B/\lambda^2$) and the thickness measured by XRR (133 nm) as seeds. The same procedure was applied to fit the optical properties of the monolayers (the model used was the Forouhi-Bloomer for the titanium dioxide)[46] and the parameters of the ITO layer previously determined were fixed. The bilayers formed by MTTF on dense titania were modeled by the same scheme, and each layer was fitted individually varying all the parameters. Finally, some of the parameters were fixed and the optical properties of both layers were fitted together in order to obtain the real and imaginary components of the refractive index ($n(\lambda)$ and $k(\lambda)$), and the thickness after an iterative procedure.

Environmental Ellipsometric Porosimetry (EEP). Water adsorption−desorption curves (at 298 K) were measured by Environmental Ellipsometric Porosimetry (EEP, SOPRA GES5A). EEP is a very powerful technique that allows assessing the porosity of the mesoporous films that is difficult to determine otherwise.[47] The experimental device is based on the coupling of a pressure controlled chamber and a spectroscopic ellipsometer. Briefly, film thickness and refractive index values were obtained from the ellipsometric parameters Ψ and Δ under nitrogen flux containing variable water vapor pressure, P; P/P_o was varied from 0 to 1 (P_o being the saturation water vapor pressure at 298 K). Optical properties of the mesoporous structure were first obtained from measurements at P/P_o = 0, which is an effective index resulting of the combination of the oxide walls and the air inside the pores. The oxide wall refractive index was calculated using a two-component (air−oxide) Bruggeman effective medium approximation:[48]

$$f_a\left(\frac{n_a^2 - n_e^2}{n_a^2 + 2n_e^2}\right) + f_w\left(\frac{n_w^2 - n_e^2}{n_w^2 + 2n_e^2}\right) = 0$$

Table 1. Structural Characteristics of All Samples[a]

						thickness FE-SEM (nm)		thickness SE (nm)	
sample	pore arrangement	a (FE-SEM)	a (GI-SAXS)	a (TEM)	thickness XRR (nm)	D	M	D	M
D3					49 ± 2	47 ± 1		46 ± 1	
D5					24 ± 5	NA		22 ± 1	
M3	*Im3m* local	15 ± 1	NA	NA	190 ± 10		180 ± 5		200 ± 5
M5	collapsed				250 ± 20		165 ± 5		194 ± 5
D3M3	*Im3m*	16 ± 1	16.5 ± 0.5	NA		50 ± 1	150 ± 5	63 ± 1	147 ± 5
D5M3	*Im3m*	15 ± 2	16.6 ± 0.5	NA		46 ± 1	146 ± 5	49 ± 1	144 ± 5
D3M5	grid-like	NA	NA	16.7 ± 0.5		45 ± 1	138 ± 4	42 ± 1	136 ± 5
D5M5	grid-like	NA	NA	16.4 ± 0.5		53 ± 1	144 ± 5	58 ± 1	146 ± 5

[a] a = cell parameter of cubic *Im3m* structure; NA = data was not measured or could not be measured; empty cells correspond to meaningless values.

where n_e = effective refractive index of the MTTF, measured at $P/P_o = 0$, n_a = air refractive index ≅ 1, n_w = TiO_2 walls refractive index, f_a = porosity (air volume fraction), and f_w = wall oxide volume fraction = $1 - f_a$.

To determine the wall oxide refractive index (n_w), it is necessary to measure the effective index at 0% RH (n_e) and the film porosity (f_a), while considering the refractive index of air (n_a = 1). The n_w was determined at 630 nm for the samples thermally treated at the different temperatures.

The water volume adsorbed at each P/P_o value V_{ad} was obtained by modeling the refractive index obtained according to a three-components (water−air−oxide) effective medium approximation (Lorentz−Lorentz). Adsorption−desorption isotherms were plotted using the obtained water volume, and considering that it corresponds to the volume adsorbed by the porous film at each P/P_o. To model the refractive index at each point, the same procedure as in the previous section was applied. Optical properties at $P/P_o = 0$ were fitted first. The parameters of dense layers (ITO and dense titania in bilayers) were fixed in the isotherm adjustment due to the lack of change with the RH.

From the measured adsorption−desorption isotherms, pore sizes distributions were obtained using models based on the Kelvin equation (see Supporting Information, Figure S2), considering the respective contact angles.[39,49] The contact angle of water to the films was determined by depositing a droplet directly on top of the sample using a Ramé-Hart 190 CA, and image analysis with Ramé-Hart DROPimage software. The measurement was repeated at least 5 times.

Surface Characterization. *Field Emission-Scanning Electron Microscopy (FE-SEM).* FE-SEM images were obtained with a ZEISS LEO 982 GEMINI field emission electron microscope in the secondary-electron mode, using an in-lens detector to improve resolution (CMA, Facultad de Ciencias Exactas y Naturales, UBA).

Samples were supported in two different ways according to the desired type of images, top or side view. Top view samples were cut with a diamond tip in small squares and added to an adhesive carbon tape above an aluminum support. For the side view samples the preparation was analogous but the adhesion was made in an L shape aluminum support.

Mesostructure Characterization. *Transmission Electron Microscopy (TEM).* TEM images were collected using a Philips EM 301 transmission electron microscope operated at 60 kV (CMA, Facultad de Ciencias Exactas y Naturales, UBA). Samples were obtained by scratching the films from the substrate and depositing them on carbon-coated copper grids.

GI-SAXS. Grazing incidence-small-angle X-ray scattering measurements were performed at the D10A-XRD2 beamline of Laboratório Nacional de Luz Síncrotron (LNLS), Campinas, SP, Brazil using a six circles Huber diffractometer (λ = 1.5498 Å) and a PILATUS detector. The incident angle was fixed at 0.23°θ with an integration time of 200 s. The obtained data was analyzed using the FIT2D program.[50]

TiO_2 Crystallization Studies. *Grazing Incidence X-ray Diffraction (GI-XRD).* The GI-XRD experiments were performed at the D10A-XRD2 beamline of LNLS using a six circles Huber diffractometer (λ = 1.5498 Å). GI-XRD measurements were performed by keeping the incident angle fixed at 0.3°. The scattered X-ray beam was recorded by moving the detector along the goniometer circle in the 2θ range between 23 and 29°, corresponding to the [101] reflection of anatase. The incident angle was chosen after the calculation of the attenuation length of the samples, so the X-rays penetrate approximately half of the sample thickness, which results in higher diffracted intensities from the film compared to the substrate.

The crystallite sizes of the thermally treated TiO_2 samples were estimated from the diffraction patterns using the Debye−Scherer formula[51]

$$t = \frac{0.9\lambda}{B\cos\theta_B}$$

where t is the crystallite size, λ is the wavelength of X-rays, B is the corrected full width at half-maximum of the peak, and θ_B is the Bragg's diffraction angle.

Selected Area Electron Diffraction (SAED). SAED data was collected using a Philips CM 200 Super Twin transmission electron microscope operated at 200 kV with EDAX (CAC, CNEA) . Samples were the same as those from TEM measurements.

Photodegradation of Methylene Blue (MB) in Aqueous Solution. MTTF were immersed in 5 μM MB aqueous solution (15 mL) in the dark for at least 3 h to ensure complete access of the solution to the full extension of the pores. The photodegradation of MB was conducted by irradiation of the surface while submerged in the MB solution under stirring with a UV lamp (Philips, λ_{max} = 360 nm, 400 W) at a constant distance for all samples to ensure same irradiation. The absorbance of the MB solution (at λ = 662 nm) versus irradiation time (10−15 min intervals) was measured using a Hewlett-Packard 8453 spectrophotometer in transmission mode. The amount of MB decomposition was determined by the Lambert−Beer equation (ε = 73004 M^{-1} cm^{-1} at 662 nm), and normalized by the exposed area.

RESULTS AND DISCUSSION

As mentioned above, materials control and design are highly relevant for the evaluation of potential applications of the given films. The challenge for real materials design remains, however, in the interdependence of the desired properties.[17] Upon films preparation, a careful study of the films must include an in-depth analysis of the relations arising between the observed materials features. In the next section each aspect (pore order, porosity and crystallinity) is evaluated systematically while assessing the causes and effects of mesoporosity, accessibility and crystallinity.

Structural Characterization. After deposition, all the obtained samples were transparent and optically homogeneous. In general, it is observed that mesoporous samples are more delicate and easily scratchable when prepared onto bare ITO. The thickness of the prepared layers was characterized by three different techniques: SE, XRR, and cross-section FE-SEM (Table 1). In all cases, thicknesses obtained by SE are in very good agreement with those obtained by XRR and FE-SEM (within 10%). The two latter techniques yield values that are model-independent, therefore, a good correlation of the ellipsometric

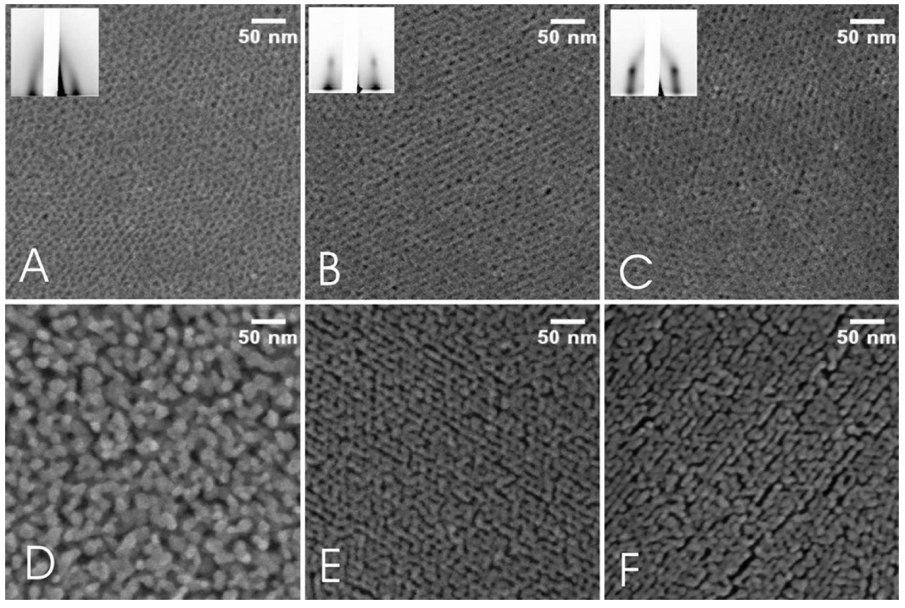

Figure 1. FE-SEM images of MTTF deposited on different substrates: (A) M3, (B) D3M3, (C) D5M3, (D) M5, (E) D3M5, and (F) D5M5. Insets: GI-SAXS patterns.

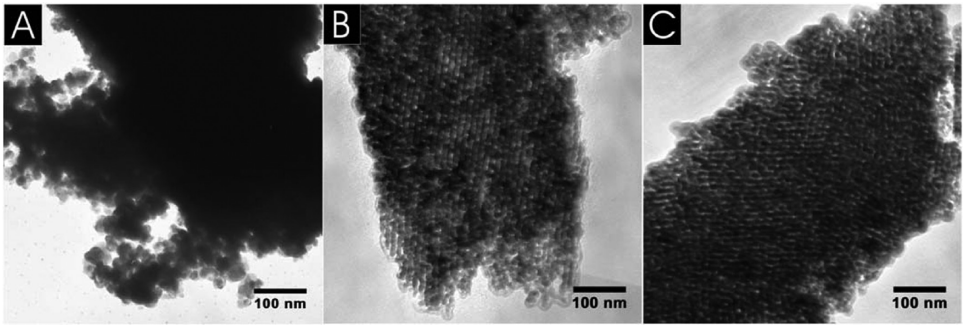

Figure 2. TEM images of (A) M5 and top layers of (B) D3M5 and (C) D5M5.

results are a clear indication of the strength of the SE model that becomes particularly convoluted for samples containing more than one layer.

The mesoporous layers are somewhat thinner when they are prepared on top of a dense layer (140−150 nm for DyMx vs ∼200 nm for the Mx), most likely an effect of the poorer wetting properties of the bare ITO compared to a thin compact TiO_2 layer.[30,52,53] The resulting films thicknesses depend not only on the dip-coating conditions (withdrawal rate, ambient humidity and temperature) but also on the affinity of the solution to the substrate surface where a more hydrophilic surface (dense TiO_2 in this work) would allow for a better wettability of the ethanolic titania solution.

Figure 1 shows representative FE-SEM top view images and GI-SAXS patterns of MTTF deposited on different substrates and submitted to different thermal treatments. Single mesoporous layers deposited on bare ITO and treated at 350 °C (M3), present systematically a locally organized mesostructure; in some regions, this local order resembles a cubic *Im*3*m* mesophase (the *a* values reported in Table 1 are extracted from these regions). These samples present well-defined *z*-directional arrangement of pores, as demonstrated by the intense out-of-plane XRD signal observed at $2\theta = 1.86°$ (see Supporting Information, Figure S3). For higher temperature treatment (M5, see Figure 1D), the local pore arrangement is disrupted and gives rise to a collection of randomly packed crystallites presenting disorganized mesoporosity. Consistently, MTTF deposition onto bare ITO leads to the sequence: local order at low temperatures, and mesostructure collapse at higher temperature treatment. In some regions, and depending on the sample type, a structure presenting local pore order with larger interpore distance (∼18 nm) has been observed for M5 (see Supporting Information, Figure S4), suggesting that collapse is preceded by reorganization of the inorganic walls and pore widening.

Alternatively, when MTTF are deposited onto a dense TiO_2 layer previously placed on top of the ITO substrate, extended regions with highly oriented mesostructure ordering are reproducibly observed. This is in excellent agreement with previous work that reported that adding a titania thin dense layer leads to improved mesostructure ordering, which is difficult to achieve on bare ITO due to interfacial incompatibility.[30] For mesoporous films onto the dense layer treated at 350 °C (D3M3 and D5M3, see Figure 1B and 1C), a well-organized *Im*3*m* pore structure is obtained, according to the GI-SAXS and FE-SEM information. Exposure of these films to higher temperatures (D3M5 and D5M5, Figure 1E and 1F) produces a grid-like arrangement of pores. Grid-like structures have been previously reported for high temperature treated mesoporous TiO_2 films deposited onto Si substrate and they have been associated to extensive crystallization of the inorganic walls into the anatase

phase.[14,28] However, there is no record of such organized films onto substrates like glass or ITO so far.

The cubic *Im3m* lattice parameters *a*, obtained from the GI-SAXS data, TEM and FE-SEM, when available, are presented in Table 1 ($a = \sqrt{2}d_{(-110)}$ for a cubic lattice; *a* represents the interpore distance in local-order samples). The *a* values for the MTTF prepared on the modified ITO/D substrate are somewhat similar and agree with previously reported lattice parameters for MTTF on Si substrate.[14,28]

It must be noticed that thermal treatment to the bottom dense layer has no appreciable effect on the pore order quality of the mesoporous top layer, for example, both D3M3 and D5M3 show top layer pores organized in an *Im3m* fashion, with similar characteristic distances. Therefore there is no need to produce highly crystalline dense layers (D5) to produce highly organized top mesoporous films, D3 films result in an already adequate surface for obtaining highly organized MTTF.

The evolution of pore organization and mesostructure upon thermal treatment was confirmed by TEM (Figure 2). The images show the presence of vertically superimposed pores that confirm the presence of organized pore arrays with noncollapsing *Im3m*-derived mesostructure for DyM5 samples, while the mesoporous layer on bare ITO treated at 550 °C shows a total collapse of the mesostructure (Figure 2A).

Cross-section FE-SEM images of D3M3 and D5M3 samples are presented in Figure 3. The different layers are easily identifiable due to their electronic contrast, allowing the measurement of the reported thicknesses presented in Table 1. Structural differences of the layers for the different temperature treatments can also be clearly observed from the images. The dense titania and the ITO layers appear to be more compact and homogeneous than the top porous layers that reveal accessible pore systems with high interconnection. This arrangement is composed of piled up interconnected mesopores; even if the image resembles "vertical channels", it is fully compatible with the projection of an *Im3m* mesostructure along a (110) direction (see Figures 2B and C). Thermal treatment at 550 °C leads to reorganization, as observed in Figure 1, and mesostructure evolution to a grid-like structure, which is in fact comprised of vertically oriented channels that permit a full vertical connection and accessibility along the film thickness (see Supporting Information, Figure S5).[14,17,35] Exposure of dense titania layers to higher temperature yields a disordered structure that might be related to rapid growth at higher temperatures with nucleation being the main barrier, as proposed by Kirsch et al. in the so-called "popcorn" mechanism.[26] In the case of confined crystallite growth, such as the one taking place in mesoporous films, crystallite size is limited by the topology of the pore system.[25] On the contrary, for dense films, growth can proceed and lead to fast, extended growth, therefore leading to an expanded, irregular pore system.

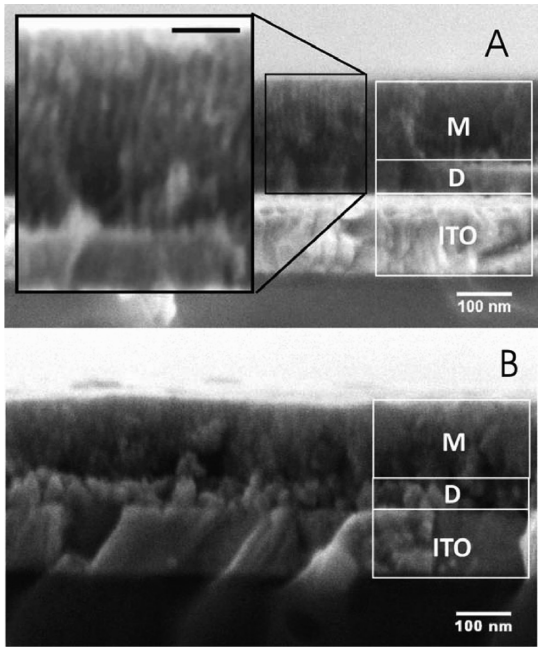

Figure 3. FE-SEM cross-section image of (A) D3M3 and (B) D5M3. Selection: Zoom of mesoporous/dense bilayer (scale bar 50 nm).

Porosity and Pore Size Distributions. The water adsorption/desorption isotherms obtained by EEP are shown in Figure 4 for all porous samples. The observed curves present well-defined capillary condensation pressure and hysteresis loops characteristic of mesoporous systems with high pore volume and narrow pore size distribution.[54,55] A first glance at the isotherm position and shape for samples deposited on different surfaces and submitted to different thermal treatment allows to rapidly recognize the importance of the nature of the substrate surface, and the significant pore reconstruction that takes place at higher temperatures. From a detailed comparison of all isotherms in Figure 4 it is evident that: a) the mesopore volume of samples depends on the surface that is deposited onto; b) the thermal evolution depends on the deposition surface; c) for all samples, there is a remarkable change of the pore shape after thermal treatment at 550 °C. These three aspects reflect the crucial role of the substrate surface quality in the thermal evolution and development of porosity and crystallinity of the sample.

Figure 4A reveals that MTTF prepared on top of bare ITO surface present similar accessible porosity (~39–40%) for both thermal treatments (M3 and M5). Alternatively, for samples treated at 350 °C, D3M3 and D5M3, porosities of ~30% are obtained. When bilayered samples are exposed to 550 °C (D3M5 and D5M5), the pore volume significantly increases to almost 50% (Figure 4B). The nature of the dense layer (i.e., dense layer with different thermal treatment) has little impact on the accessible volume of the top layer; this is coincident with the SEM and TEM information, in which no significant structural difference could be observed when changing the thermal treatment of the dense titania underlayer. The difference in pore volume for samples treated at 350 °C can be traced back to the significant role that the substrate surfaces play in the film formation process. In the case of silica, Klotz and co-workers have reported that film texture and contraction of the ordered mesostructure is indeed influenced by the choice of substrate.[56,57] Even if this complex problem has not yet been systematically undertaken in the literature of mesoporous films, factors like substrate roughness or chemical affinity have been proposed to influence the organization and the contraction upon postsynthesis treatment. These factors can have a marked effect in the pore volume and pore size distribution, as well as modification of the film mechanical properties. Indeed, Angelomé et al. found that MTTF with similar thickness deposited onto silicon presented a 25% increase in pore volume with respect to those deposited on glass.[41]

Regarding the change in pore volume upon high thermal treatment that is only observed for the titania-covered substrate, the obtained results are in excellent agreement with those

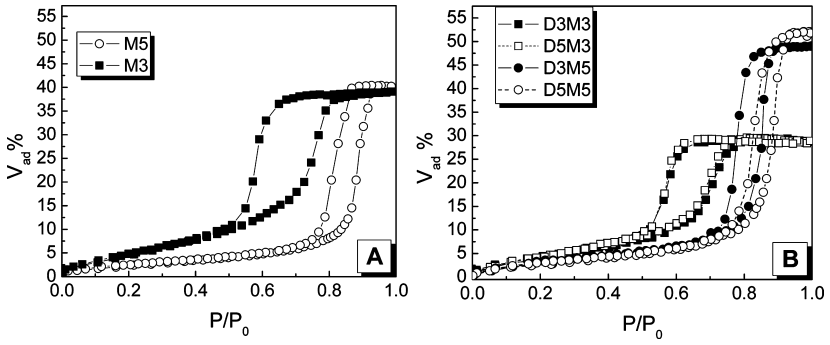

Figure 4. EEP isotherms of single mesoporous layers (A) and bilayers composed of a mesoporous titania on a dense titania underlayer (B). Sample names are indicated on each of the panels.

reported for MTTF deposited on silicon substrates. Sakatani et al. proposed that the pore system was not entirely opened to water adsorption at 300−350 °C, and that thermal treatment at temperatures higher than 400 °C was needed to fully open the pore system.[14] Bare ITO-supported MTTF present a different evolution upon heating. Analysis of the pore volumes and diameters in Table 2 shows that in the case of ITO-supported MTTF there is a slight increase in pore volume (~2.5%), while for samples with the dense titania layer, the pore volume is increased by almost 50%. Contrarily, the pore diameter increase is similar for both systems (~20%). These results suggest that the reconstruction of the pore system is more extended in MTTF deposited onto the titania-modified substrates than in those deposited directly onto ITO.

Table 2. Porosity Features of Mesoporous Layers Obtained from EEP and Contact Angle Values[a]

sample	accessible porosity (%)	PD (nm)	ND (nm)	CA (deg)
D3	3.6 ± 0.2			
D5	1.2 ± 0.2			
M3[b]	39.2 ± 0.2	8.2 ± 0.5	4.5 ± 0.5	20 ± 2
M5[c]	40.2 ± 0.2	10.0 ± 0.5		23 ± 1
D3M3[b]	29.1 ± 0.2	6.7 ± 0.5	4.2 ± 0.5	21 ± 1
D5M3[b]	28.9 ± 0.2	6.4 ± 0.5	4.2 ± 0.5	21 ± 1
D3M5[c]	49.2 ± 0.2	9.0 ± 0.5		24 ± 4
D5M5[c]	52.7 ± 0.2	11.7 ± 0.5		25 ± 5

[a]PD = pore diameter. ND = neck diameter. CA = contact angle. [b]Pore diameter calculated from adsorption isotherm, neck diameter calculated from desorption isotherm (H2 loop). [c]Pore diameter calculated from desorption isotherm (H1 loop).

Interestingly, systems deposited on bare or titania-modified ITO present a coincidence: the shape of the hysteresis loops changes after thermal treatment to 550 °C. Samples treated up to 350 °C present Type H2 loops, typical of a three-dimensional pore array with restrictions. Thermal treatment to 550 °C leads to two effects: the capillary condensation steps are shifted to higher pressures, and the hysteresis observed corresponds to H1 loops. It has to be noticed that neither the film thickness nor the contact angles vary significantly upon heating to 550 °C in all cases (Tables 1 and 2). Therefore, it can be assumed that the pore anisotropy does not change appreciably for both thermal treatments and that the interactions between the pore surface and water are kept reasonably constant. These two quantities are important in order to calculate the pore size distributions. Average pore diameters are presented in Table 2. For the 350 °C treated samples, pore diameter was calculated from the adsorption curves, due to the presence of an H2 loop, characteristic of interconnected pores with restrictions. In this kind of samples, it is considered that the adsorption isotherm reflects equilibrium, and thus a neck diameter can be obtained from the desorption curves (also reported in Table 2). In the case of the 550 °C treated samples, the pore diameter values were estimated from the desorption curve, since the desorption process corresponds to equilibrium for H1 isotherms.[55] An increase in pore diameter after 550 °C treatment can be observed in all samples. This size increase is due to the sintering effect that results in surface reconstruction with material from the neck diffusing into the pore walls upon thermal treatment yielding open channel type pores.[14]

EEP was also performed for the dense (nonmesoporous) layers (see Supporting Information, Figure S6). Even though samples were intended to be compact TiO_2 layers, some degree of residual microporosity is always observed for sol−gel prepared samples (see Table 2).[40]

The MTTF pore evolution observed upon heating to 550 °C is a consequence of complex phenomena that takes place at different rates in each of the systems. The diverse adsorption/desorption behavior for films at various thermal treatments is consistent with the structural differences observed by FE-SEM and with previously reported results.[14] From the structural point of view, and taking into account the results presented so far, it can be observed that while the organized mesostructure deposited directly onto ITO is disrupted upon heating, no significant changes of mesostructure dimensions take place in the films deposited onto a titania-modified ITO. In the first case, no appreciable change in pore volume is observed when exposed to elevated temperatures, but a significant pore coarsening and shape change take place, according to the EEP and FE-SEM information. These observations might be a result of an enhanced transport of matter in high temperature thermally treated samples that enlarges the mesopores with no significant densification of the inorganic walls. The bare ITO surface seems to hinder anatase crystallization, as previously reported for MTTF single layers.[15] In addition, the ITO has some deleterious effect in the mesoporous structure, probably due to differences in the wetting properties. On the contrary, when a dense titania underlayer is present, diffusive sintering is now accompanied by wall densification through efficient nanocrystalline anatase growth; consequently, the pore volume increases remarkably. A grid-like structure is obtained after a significant pore shape rearrangement.[14] The slight difference in pore sizes of samples D3M5 and D5M5 could be attributed to the increased roughness of D5 layer compared to D3 layer (see Supporting Information Figure S5). Crystallization enhancement due to the modification

of ITO has been observed before;[22] however, no details in the pore evolution were provided in that report. Here, the crossed experiments demonstrate that the titania underlayer facilitates the evolution of the wall material to denser titania, which is efficiently transformed into the anatase phase upon matter transport and pore enlargement. In addition, the accessible pore volume increases with further thermal treatment, (i.e., porosity is larger for DyM5 than for DyM3), suggesting that wall densification is not complete in samples thermally treated at low temperature.

Interestingly, the cubic samples studied in this work present a different thermal behavior with respect to the one reported in 2D hexagonal MTTF by Choi et al.[58] In the latter case, an evolution from larger, cylindrical (with H1 hysteresis) to smaller, ink-bottle mesopores (with H2 hysteresis) is observed, and attributed to anatase growth, presumably within the pores. The thermal evolution of the pore system is closely tied to the mesostructure as evidenced from the comparison of results obtained for a 2D hexagonal system and those reported here and in work by Sakatani et al on *Im3m*-derived samples.[14] It is clear that the crystallite growth is limited by the topology of the pore system,[25,26] at least at moderate temperatures in which material diffusion and crystal growth processes are reasonably slow and can be controlled.[17]

Crystallization Studies. The degree of crystallization upon thermal treatment was assessed by GI-XRD. For the dense layers, the characteristic anatase crystalline peak from the (101) plane at 2θ−25.5° was chosen, and its evolution followed for samples treated at high temperature, D5 (Figure 5). Similarly, an anatase

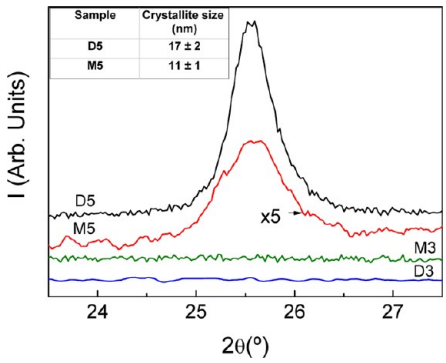

Figure 5. Diffractograms of samples M3, D3, M5, and D5. (Curves have been translated vertically for clarity.)

signal was observed only for an M5 single layer. Crystallite sizes of both samples calculated from the diffraction patterns yield 17 and 11 nm, respectively (see Figure 5, inset). The anatase crystallite size for the mesoporous layer is expectedly smaller than the obtained for dense layers because of the constrained crystallite growth beyond the pore wall limits. No appreciable anatase signal was observed for the low temperature treated samples (D3 and M3). It has to be pointed out that XRD presents some limitations to assess very small anatase-like local domains that impart distinct electronic properties. Previous work has carefully quantified a fraction of about 40% of such anatase-like domains for MTTF treated at 350° on ITO similar to the ones presented here.[15]

Conversely, bilayered samples for all combination of temperature treatments (DyMx) present the anatase (101) diffraction peak at 2θ~25.5° (see Supporting Information, Figure S7). Such signal may arise from either the bottom-dense layer or the top-mesoporous or even a combination of both since the incident grazing angle beam allows total film penetration. It is noticeable, however, that a signal for the D3M3 marks an important crystallinity difference with respect to single D3 and M3 films, which are essentially amorphous by XRD.

All MTTF prepared onto dense titania-modified ITO were further studied by SAED of the mesoporous layers (the corresponding TEM images were presented in Figure 2 B and C, showing the selected sample zone for SAED where only the mesoporous layer is probed). Only diffuse rings characteristic of amorphous materials were observed for mesoporous layers treated at low temperatures (Figures 6A and 6C). Contrarily, for D3M5 and D5M5 samples, diffraction rings characteristic of a polycrystalline material can be observed (Figures 6B and 6D). Extensive crystallization of MTTF appears only for samples treated at 550 °C, independently of the thermal treatment of the dense layer. It has been proposed that upon thermal treatment, an appreciable migration of ions from the ITO layer can take place preventing crystallization of the mesoporous titania walls.[15,23] In this case however, the dense TiO_2 underlayer may be preventing this unwanted process acting as a barrier for ion migration. The modification of the ITO surface by a dense layer previous to the mesopore formation is the key for obtaining a stable inorganic framework that can yield elevated crystallinity upon thermal treatment.

Optical Properties. Modeling of the SE signal yields the optical components of the refractive index, $n(\lambda)$ and $k(\lambda)$ as shown in Figure 7A. The optical band gap (E_g) can be extracted from $k(\lambda)$ by extrapolating the straight line portion of the $(\alpha h\nu)^{1/2}$ versus $h\nu$ plot (Figure 7B), where α is the optical absorption coefficient; the extracted data is shown in Table 3. The E_g of the dense layers tends to decrease for higher thermal treatments approaching the reported literature values for bulk anatase (3.02−3.19 eV).[59] For all mesoporous layers, the same trend is observed: E_g values always decrease for higher temperature exposures. Higher optical band gap energies are attributed to quantum size effect of TiO_2 nanocrystals with sizes of less than 10 nm due to the confinement of the pore walls dimensions.[2,60−62] Reportedly, the indirect band gap decreases with increasing annealing temperature as a result of an extended anatase fraction and an increase in grain size.[63−66] Hereby, it is fair to assume that the calculation of E_g by adjustment of the optical parameters is a good confirmation of the premise formulated throughout this work stating that thermal treatments of MTTF or dense titania layers would necessarily yield films with improved crystalline character. The remarkable result is, however, the effect of modifying the ITO by a thin dense titania layer on the resulting E_g. Band gaps of films onto ITO/D surfaces yield smaller values than their analogous counterparts prepared onto ITO (e.g., 3.42 eV for D3M3 versus 3.64 eV for M3), independently confirming that the simple introduction of the interfacial dense layer facilitates the crystallization of the titania pore walls. Consistently too, there is little effect of the dense layer nature onto the E_g of the top mesoporous layers, being similar for samples treated at the same temperature whether the dense layer is crystalline or not.

The refractive indexes at 630 nm are also reported in Table 3. The n_e values obtained directly from the EEP measurements at RH% = 0 were corrected considering the contribution of the air contained in the pores, to obtain the refractive index of the titania walls (n_w). The refractive index is material dependent and is also an indication of the amorphous or crystalline character of the films. For bulk anatase, the amorphous titania n values are

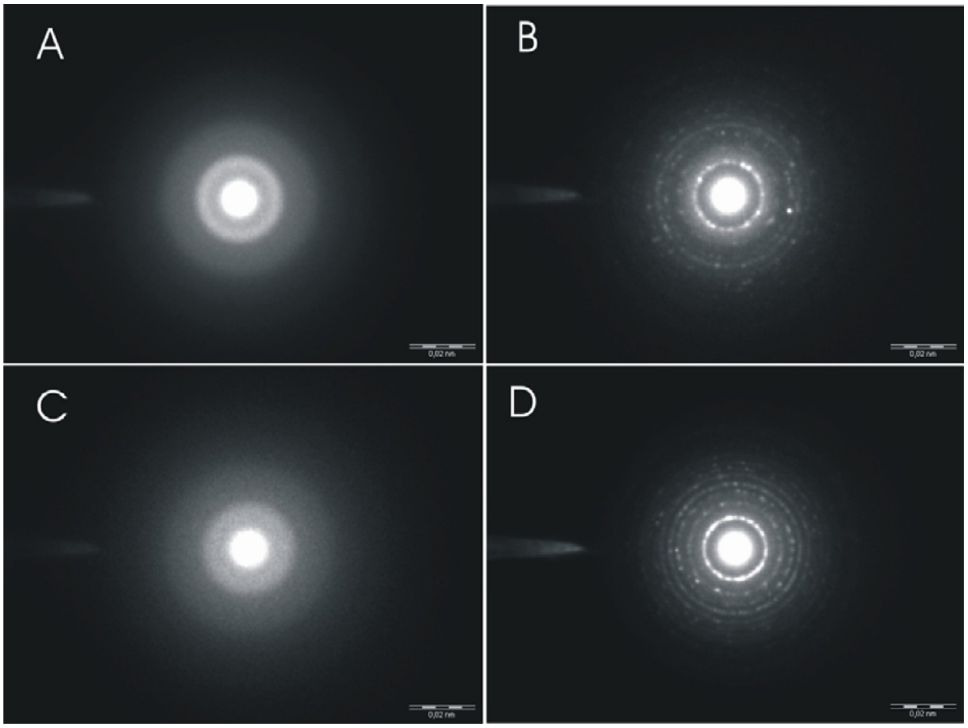

Figure 6. SAED patterns of MTTF deposited onto titania-coated ITO: (A) D3M3, (B) D3M5, (C) D5M3, and (D) D5M5.

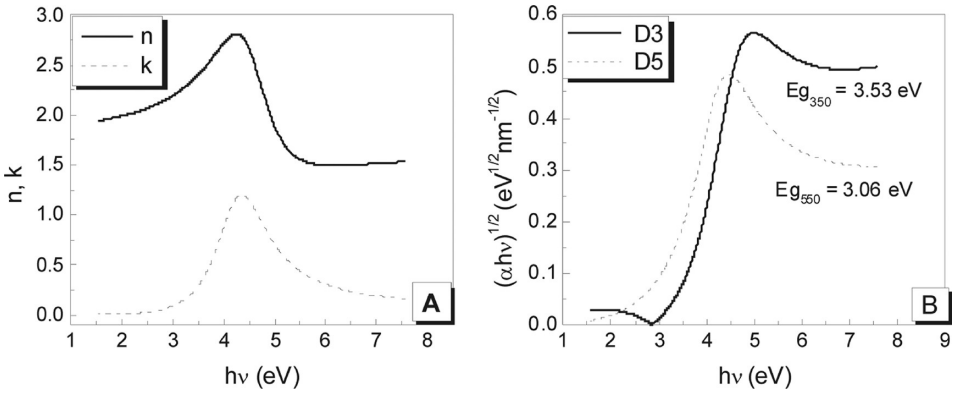

Figure 7. (A) *n*, *k* curves for D5 sample. (B) Indirect band gap determination.

Table 3. Indirect Band Gaps Values Obtained from Ellipsometric Measurements[a]

	E_g (eV)				
sample	dense layer	mesoporous layer	n_e	n_w	n_w/n_{an}
D3	3.53 ± 0.03		1.96 ± 0.02	2.00 ± 0.02	0.79
D5	3.06 ± 0.02		2.38 ± 0.02	2.39 ± 0.02	0.95
M3		3.64 ± 0.03	1.54 ± 0.01	1.91 ± 0.02	0.76
M5		3.48 ± 0.03	1.49 ± 0.01	1.85 ± 0.02	0.73
D3M3	3.18 ± 0.02	3.42 ± 0.02	1.53 ± 0.01	1.76 ± 0.02	0.70
D5M3	3.05 ± 0.03	3.49 ± 0.03	1.59 ± 0.01	1.89 ± 0.02	0.75
D3M5	2.73 ± 0.02	3.36 ± 0.02	1.55 ± 0.01	2.14 ± 0.02	0.85
D5M5	2.96 ± 0.02	3.37 ± 0.02	1.52 ± 0.01	2.18 ± 0.02	0.87

[a] n_e = Refractive index for the mesoporous TiO_2 layer at vapor pressure (P_v) = 0. n_w = Refractive index calculated for the mesoporous TiO_2 walls (except for D3 and D5 samples) at the same P_v. n_w/n_{an} = ratio between the calculated refractive index and the bulk anatase reported value [n_{an} = 2.52].[67] All reported *n* values are for wavelengths of 630 nm.

reportedly lower than the crystalline phase, n_{an} = 2.52,[67] that is, the refractive index decreases when the fraction of crystalline anatase decreases. To rationalize the trends of the prepared materials, the ratio between the titania walls refractive index and the reported bulk anatase is shown (Table 3). As the ratio becomes closer to 1, the titania resembles the bulk anatase in terms of the amount of crystallization. In this manner, the ratio n_w/n_{an} can be understood as a crystallization ratio. It is first

dx.doi.org/10.1021/am300990p | ACS Appl. Mater. Interfaces 2012, 4, 4320−4330

noticed that the increased crystallization ratio of the dense layer upon exposure to 500 °C almost resembles that of the bulk anatase. Conversely, for mesoporous materials, it is evident that to have a real increase in the crystallization ratio, it is necessary to combine the modification of the ITO surface with the temperature treatment. MTTF prepared onto the dense titania on ITO show crystallization ratios of 0.85−0.87 for 550 °C treatment and 0.70−0.75 for 350 °C. No such trend is observed for the MTTF prepared directly on ITO, which present values in the 0.73−0.76 range, independent of the heating temperature. This latter aspect is also consistent with the observed evolution of the pore systems, presented in section 2. In the case of ITO-deposited films, pore coarsening upon thermal treatment is not accompanied by densification and crystallization of the inorganic walls; therefore, it is natural that the pore volume remains essentially constant. On the other hand, the densification observed by EEP with an increase in the accessible volume for the MTTF deposited onto the ITO/D substrates is confirmed by the notable increase in crystallization ratio for samples heated at 550 °C.

The combined results of the previous sections consistently indicate that the porosity features (i.e., pore volume, diameter, and pore array symmetry) along with the thermal evolution of MTTF are strongly dependent on the nature of the substrate surface. The modification of the ITO interface by a dense TiO_2 film produces a surface that improves wetting, mechanical and porosity properties of the MTTF. In particular, when mesoporous films are deposited onto titania-modified ITO, an efficient wall densification process is accompanied by crystallization which is intimately related to the structure of the initial mesopore framework. Hence, the mesostructure is determinant in the fate of the pore size and shape, as well as the wall thickness and crystallite size after thermal evolution. In summary, as a result of a controllable process, an organized pore framework with nanocrystalline walls and high thermal stability is obtained, as demonstrated through the cross characterization via XRD, EEP, and SE measurements.

Photocatalytic Performance. The photocatalytic activity of all mesoporous films was tested by the decomposition of methylene blue (MB) in contact with the TiO_2 surface. The decomposition reaction initiates upon the absorption of a UV photon by the TiO_2 that creates an electron−hole pair at the surface with sufficient energy to initiate the oxidative degradation process of an MB molecule. Figure 8 shows the decrease in the absorbance with irradiation time that indicates the photodegradation of the MB. The amount of the decomposed MB is calculated from the reduction of the corresponding absorption band and normalized by the exposed area of the TiO_2 film. Figure 9 shows the photocatalytic activity for all samples. The best performance was achieved by the DyM5 samples that present a grid-like structure with extraordinary high accessible pore volume and extended crystallization, as discussed in earlier sections. All these features contribute in a positive manner to the observed enhanced photocatalysis. Increased pore accessibility and pore order permits an efficient MB diffusion into the depths of the pore system, increasing the amount of molecules in contact with the titania surface. In addition, the increased amount of anatase fraction has a direct impact on the photocatalytic activity because of the appropriate energetics (E_g) for pollutant decomposition.[14,15,21] The low crystallinity fraction of the samples M3 and D3 has a negative impact on the photocatalytic activity that is worse for the dense layer due to the lack of pore accessibility. D5 and DyM3 samples show intermediate photodegradation capacity for opposing reasons. While D5 contains a great fraction of crystalline titania it does not offer enough accessible volume; contrarily, DyM3 is less crystalline but contains higher accessible volume. It is clear then that the full characterization of the samples described in earlier sections provided a sensible direction in terms of predicting the capacity of the material for real-life applications.

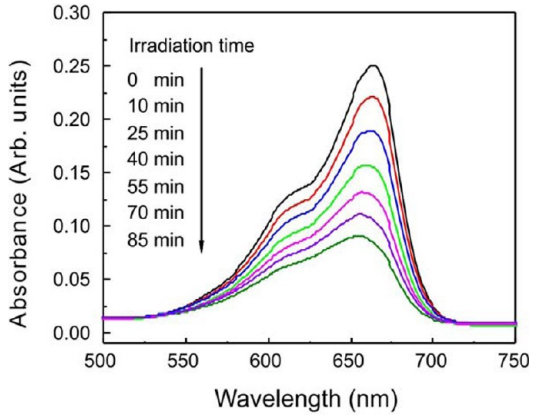

Figure 8. Absorption spectra of MB solution upon UV irradiation time of the D5M5 sample.

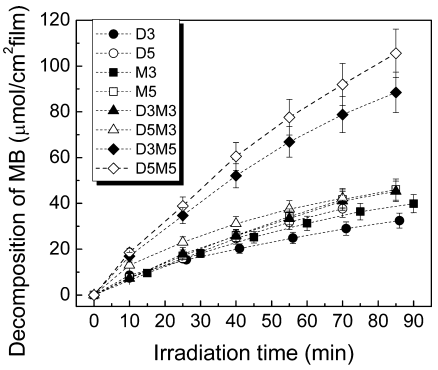

Figure 9. Photodegradation of MB over various MTTF under UV light irradiation.

The photocatalysis studies presented here clearly demonstrate that an optimum of ordered and highly accessible pores with great extent of anatase fraction yield the best materials for photodegradation applications, as observed previously in Si-supported[15,68] or powdered titania.[68] Importantly, these properties can only be achieved onto a transparent ITO substrate by simply introducing a thin dense titania buffer layer, after a brief thermal treatment. Although it is not necessary to have a conductive electrode to develop photocatalytic activity, this behavior reflects an improvement in electronic properties (carrier availability, interconnectivity) that can be extended to other practical applications such as photoelectrocatalysis,[15] that is, photocatalysis under bias, lithium insertion electrodes or solar cells.

CONCLUSIONS

Highly ordered, high mesopore volume (25−50%) and tuned mesoporous nanocrystalline titania films were prepared onto modified-ITO transparent substrates. The effect of a nonporous underlayer and a short ("flash") thermal treatment in the

porosity and crystalline wall character was fully assessed by a set of crossed techniques. A thin TiO_2 dense layer deposited on top of the ITO surface improves the film wetting properties, reduces the film−substrate strain and prevents unwanted ion migration into the mesoporous titania upon thermal exposure. If these factors are not controlled, wall crystallization is not controlled, and can either be hindered or provoke the collapse of the mesoporosity.

The "flash" process studied here permits a fast yet controlled wall crystallization, while minimizing mesostructure disruption. The final mesopore architecture is generated after a significant densification of the inorganic walls, leading to mesopores with little or no restrictions, as well as a high degree of wall crystallization into anatase.

To our knowledge, this is the first time that grid-like mesostructures with high pore organization, accessibility and nanocrystalline walls are produced on transparent ITO substrates. The photodegradation studies demonstrate that MTTF with large, accessible pores and crystallinity present an optimized performance. The outcome of this work is also significant for the creation of designed MTTF with optimized pore size and crystallinity for DSSC or hybrid solar cells with improved properties.

■ ASSOCIATED CONTENT

Supporting Information

Low angle XRD for the M3 sample, FE-SEM images of different M5 samples, EEP for dense layers D3/5, and XRD for bilayers. FE-SEM cross-section images of D3M5 and D5M5. This information is available free of charge via the Internet at http://pubs.acs.org/.

■ AUTHOR INFORMATION

Corresponding Author

*E-mail: gsoler@cnea.gov.ar.

Present Address

[†]Gerencia Investigación y Aplicaciones, CAC, CNEA.

Notes

The authors declare no competing financial interest.

■ ACKNOWLEDGMENTS

The authors acknowledge financial support from ANPCyT (PICT 2008-1848, PICT 2010-0026 and PAE-37063-PME-2006-00038), University of Buenos Aires (X003), CONICET (PIP 11220100100186), Gabbos (D&G 017), and LNLS (beamline D10A-XRD2, projects 9118, 10768 and 10041). Dr. P. C. Angelomé is gratefully thanked for insightful discussions, and Boris Boaglio is thanked for assistance during the photocatalysis experiments. I.L.V. acknowledges CONICET for a doctoral scholarship. M.D.P., M.C.F., and G.J.A.A.S.I. are CONICET researchers. Both I.L.V. and M.D.P. contributed equally to this work.

■ REFERENCES

(1) Sanchez, C.; Boissière, C.; Grosso, D.; Laberty, C.; Nicole, L. *Chem. Mater.* **2008**, *20*, 682−737.
(2) Hoffmann, M. R.; Martin, S. T.; Choi, W.; Bahnemann, D. W. *Chem. Rev.* **1995**, *95*, 69−96.
(3) Zukalovà, M.; Zukal, A.; Kavan, L.; Nazeeruddin, M. K.; Liska, P.; Grätzel, M. *Nano Lett.* **2005**, *5*, 1789−1792.
(4) Coakley, K. M.; McGehee, M. D. *Appl. Phys. Lett.* **2003**, *83*, 3380−3382.
(5) Coakley, K. M.; McGehee, M. D. *Chem. Mater.* **2004**, *16*, 4533−4542.
(6) Coakley, K. M.; Liu, Y.; McGehee, M. D.; Frindell, K. L.; Stucky, G. D. *Adv. Funct. Mater.* **2003**, *13*, 301−306.
(7) Agarwala, S.; Kevin, M.; Wong, A. S.; Peh, C. K.; Thavasi, V.; Ho, G. W. *ACS Appl. Mater. Interfaces* **2010**, *2*, 1844−50.
(8) Fattakhova-Rohlfing, D.; Wark, M.; Brezesinski, T.; Smarsly, B. M.; Rathouský, J. *Adv. Funct. Mater.* **2007**, *17*, 123−132.
(9) Brezesinski, T.; Wang, J.; Polleux, J.; Dunn, B.; Tolbert, S. H. *J. Am. Chem. Soc.* **2009**, *131*, 1802−1809.
(10) Henderson, M. A. *Surf. Sci. Rep.* **2011**, *66*, 185−297.
(11) Pan, J. H.; Zhao, X. S.; Lee, W. I. *Chem. Eng. J.* **2011**, *170*, 363−380.
(12) Carreon, M. A.; Choi, S. Y.; Mamak, M.; Chopra, N.; Ozin, G. A. *J. Mater. Chem.* **2007**, *17*, 82−89.
(13) Hartmann, P.; Lee, D.-K.; Smarsly, B. M.; Janek, J. *ACS Nano* **2010**, *4*, 3147−3154.
(14) Sakatani, Y.; Grosso, D.; Nicole, L.; Boissiere, C.; Soler-Illia, G. J. A. A.; Sanchez, C. *J. Mater. Chem.* **2006**, *16*, 77−82.
(15) Angelomé, P. C.; Andrini, L.; Calvo, M. E.; Requejo, F. G.; Bilmes, S. A.; Soler-Illia, G. J. A. A. *J. Phys. Chem. C* **2007**, *111*, 10886−10893.
(16) Zhang, Y.; Xie, Z.; Wang, J. *ACS Appl. Mater. Interfaces* **2009**, *1*, 2789−2795.
(17) Soler-Illia, G. J. A. A.; Angelomé, P. C.; Fuertes, M. C.; Grosso, D.; Boissière, C. *Nanoscale* **2012**, *4*, 2549−2566.
(18) Yu, J. C.; Wang, X.; Fu, X. *Chem. Mater.* **2004**, *16*, 1523−1530.
(19) McGehee, M. D. *Mater. Res. Bull.* **2009**, *34*, 95−100.
(20) Kim, S. S.; Jo, J.; Chun, C.; Hong, J. C.; Kim, D. Y. *J. Photochem. Photobiol., A* **2007**, *188*, 364−370.
(21) Zhang, Y.; Li, J.; Wang, J. *Chem. Mater.* **2006**, *18*, 2917−2923.
(22) Štangar, U. L.; Černigoj, U.; Trebše, P.; Maver, K.; Gross, S. *Monatsh. Chem.* **2006**, *137*, 647−655.
(23) Nam, H. J.; Amemiya, T.; Murabayashi, M.; Itoh, K. *J. Phys. Chem. B* **2004**, *108*, 8254−8259.
(24) Bannat, I.; Wessels, K.; Oekermann, T.; Rathousky, J.; Bahnemann, D.; Wark, M. *Chem. Mater.* **2009**, *21*, 1645−1653.
(25) Choi, S. Y.; Mamak, M.; Speakman, S.; Chopra, N.; Ozin, G. A. *Small* **2005**, *1*, 226−232.
(26) Kirsch, B. L.; Richman, E. K.; Riley, A. E.; Tolbert, S. H. *J. Phys. Chem. B* **2004**, *108*, 12698−12706.
(27) Innocenzi, P.; MalfattiL.; Kidchob, T.; Enzo, S.; Della Ventura, G.; Schade, U.; Marcelli, A. *J. Phys. Chem. C* **2010**, *114*, 22385−22391.
(28) Grosso, D.; Soler-Illia, G. J. A. A.; Crepaldi, E.; Cagnol, F.; Sinturel, C.; Bourgeois, A.; Brunet-Bruneau, A.; Amenitsch, H.; Albouy, P. A.; Sanchez, C. *Chem. Mater.* **2003**, *15*, 4562−4570.
(29) Bass, J. D.; Grosso, D.; Boissiere, C.; Sanchez, C. *J. Am. Chem. Soc.* **2008**, *130*, 7882−7897.
(30) Uchida, H.; Patel, M. N.; May, R. A.; Gupta, G.; Stevenson, K. J.; Johnston, K. P. *Thin Solid Films* **2010**, *518*, 3169−3176.
(31) Yun, H. S.; Miyazawa, K.; Zhou, H.; Honma, I.; Kuwabara, M. *Adv. Mater.* **2001**, *13*, 1377−1380.
(32) Hwang, Y. K.; Lee, K. C.; Y.U., K. *Chem. Commun.* **2001**, 1738−1739.
(33) Grosso, D.; Soler-Illia, G. J. A. A.; Babonneau, F.; Sanchez, C.; Albouy, P. A.; Brunet-Bruneau, A.; Balkenende, A. R. *Adv. Mater.* **2001**, *13*, 1085.
(34) Alberius, P. C. A.; Frindell, K. L.; Hayward, R. C.; Kramer, E. J.; Stucky, G. D.; Chmelka, B. F. *Chem. Mater.* **2002**, *14*, 3284.
(35) Crepaldi, E. L.; Soler-Illia, G. J. A. A.; Grosso, D.; Cagnol, F.; Ribot, F.; Sanchez, C. *J. Am. Chem. Soc.* **2003**, *125*, 9770−9786.
(36) Bosc, F.; Ayral, A.; Albouy, P. A.; Guizard, C. *Chem. Mater.* **2003**, *15*, 2463−2468.
(37) Smarsly, B.; Grosso, D.; Brezesinski, T.; Pinna, N.; Boissière, C.; Antonietti, M.; Sánchez, C. *Chem. Mater.* **2004**, *16*, 2948−2952.
(38) Krins, N.; Faustini, M.; Louis, B.; Grosso, D. *Chem. Mater.* **2010**, *22*, 6218−6220.
(39) Boissiere, C.; Grosso, D.; Lepoutre, S.; Nicole, L.; Bruneau, A. B.; Sanchez, C. *Langmuir* **2005**, *21*, 12362−12371.

(40) Fuertes, M. C.; Barrera, M. P.; Plá, J. *Thin Solid Films* **2012**, *520*, 4853−4862.
(41) Angelomé, P. C. Ph.D. Thesis, Universidad de Buenos Aires, Buenos Aires, Argentina, 2008.
(42) Crepaldi, E. L.; Soler-Illia, G. J. d. A. A.; Grosso, D.; Sanchez, C. *New J. Chem.* **2003**, *27*, 9−13.
(43) Daillant, J.; Gibaud, A., Springer: Berlin, 2009.
(44) Van der Lee, A. *Solid State Sci.* **2000**, *2*, 257−278.
(45) Tompkins, H. G.; McGahan, W. A. Wiley Interscience: 1999.
(46) Forouhi, A. R.; Bloomer, I. *Phys. Rev. B* **1986**, *34*, 7018−7026.
(47) Baklanov, M. R.; Mogilnikov, K. P.; Polovinkin, V. G.; Dultsev, F. N. *J. Vac. Sci. Technol., B: Nanotechnol. Microelectron. Mater., Process., Meas., Phenom.* **2000**, *18*, 1385−1391.
(48) Bruggeman, D. A. G. *Ann. Phys.* **1935**, *416*, 636−664.
(49) Rouquerol, F.; Rouquerol, J.; Sing, K. Academic Press: San Diego, 1999.
(50) http://www.esrf.eu/computing/scientific/FIT2D/.
(51) Cullity, B. D. Addison-Wesley: MA, 1978.
(52) Fuertes, M. C.; López-Alcaraz, F. J.; Marchi, M. C.; Troiani, H. E.; Luca, V.; Míguez, H.; Soler-Illia, G. J. D. A. A. *Adv. Funct. Mater.* **2007**, *17*, 1247−1254.
(53) Fuertes, M. C. Ph.D. Thesis, Universidad Nacional de San Martín, Buenos Aires, Argentina, 2009.
(54) Gregg, S. J.; Sing, S. W., 2nd ed.; Academic: New York, 1982.
(55) Lowell, S.; Shields, J. E.; Thomas, M. A.; Thommes, M. Springer: Berlin, 2006.
(56) Chougnet, A.; Heitz, C.; Søndergard, E.; Berquier, J.-M.; Albouy, P.-A.; Klotz, M. *J. Mater. Chem.* **2005**, *15*, 3340−3345.
(57) Chougnet, A.; Heitz, C.; Søndergard, E.; Albouy, P.-A.; Klotz, M. *Thin Solid Films* **2006**, *495*, 40−44.
(58) Choi, S. Y.; Mamak, M.; Coombs, N.; Chopra, N.; Ozin, G. A. *Adv. Funct. Mater.* **2004**, *14*, 335−344.
(59) Daude, N.; Gout, C.; Jouanin, C. *Phys. Rev. B* **1977**, *15*, 3229−3235.
(60) Kormann, C.; Bahnemann, D. W.; Hoffmann, M. R. *J. Phys. Chem.* **1988**, *92*, 5196−5201.
(61) Yu, J. C.; Zhang, L.; Yu, J. *Chem. Mater.* **2002**, *14*, 4647−4653.
(62) Yu, J. C.; Zhang, L.; Zheng, Z.; Zhao, J. *Chem. Mater.* **2003**, *15*, 2280−2286.
(63) Hu, L.; Yoko, T.; Kozuka, H.; Sakka, S. *Thin Solid Films* **1992**, *219*, 18−23.
(64) Tang, H.; Prasad, K.; Sanjinès, R.; Schmid, P. E.; Lévy, F. *J. Appl. Phys.* **1994**, *75*, 2042−2047.
(65) Wang, Z.; Helmersson, U.; Käll, P. O. *Thin Solid Films* **2002**, *405*, 50−54.
(66) Mathews, N. R.; Morales, E. R.; Cortés-Jacome, M. A.; Toledo Antonio, J. A. *Solar Energy* **2009**, *83*, 1499−1508.
(67) Kingery, W. D.; Bowen, H. K.; Uhlmann, D. R. Wiley: New York, 1976.
(68) Araujo, P. Z.; Luca, V.; Bozzano, P. B.; Bianchi, H. L.; Soler-Illia, G. J. A. A.; Blesa, M. A. *ACS Appl. Mater. Interfaces* **2010**, *2*, 1663−1673.